

Star-grain rocket motor – nonsteady internal ballistics

Sonny Loncaric, David R. Greatrix *, Zouheir Fawaz

Department of Aerospace Engineering, Ryerson University, Toronto, Canada M5B 2K3

Received 20 December 2002; received in revised form 2 June 2003; accepted 9 September 2003

Abstract

The nonsteady internal ballistics of a star-grain solid-propellant rocket motor are investigated through a numerical simulation model that incorporates both the internal flow and surrounding structure. The effects of structural vibration on burning rate augmentation and wave development in nonsteady operation are demonstrated. The amount of damping plays a role in influencing the predicted axial combustion instability symptoms of the motor. The variation in oscillation frequencies about a given star grain section periphery, and along the grain with different levels of burnback, also influences the means by which the local acceleration drives the combustion and flow behaviour.

© 2003 Elsevier SAS. All rights reserved.

Keywords: Solid rocket motor; Star grain; Internal ballistic modeling; Structural vibration; Combustion instability

1. Introduction

Symptoms commonly attributed to axial combustion instability in solid-propellant rocket motors (SRMs) include the formation of a sustained limited-amplitude oscillating axial compression wave in the core flow, with an associated dc shift in base pressure in some cases. Earlier experimental findings reported in [12] illustrate that axial combustion instability symptoms can occur under certain conditions where it is evident that the motor structure influences this behaviour. Using a numerical simulation model for cylindrical-grain SRMs, predicted results in [11] illustrated the potential for explicit coupling between structural vibrations and nonsteady internal ballistic behaviour, independent of any other instability driving mechanism (e.g., augmented frequency-dependent pressure- or velocity-coupled combustion response as commonly applied by combustion instability researchers [15]; in more complex grain geometries, e.g., with segmented propellant sections, vortex shedding is also being investigated as a driving mechanism of axial wave symptoms [15]).

Greatrix [6–8] has shown that both steady and unsteady acceleration fields can significantly affect the burning rate of the solid propellant. This augmentation of the burning rate can play a key role in pressure wave development

within the motor chamber. The influence of the structural vibrations and the unsteady acceleration fields they create in the motor are thus of importance. However, nonsteady accelerations are more difficult to analyze for star-grain or other non-cylindrical configurations that are common in SRM applications, and a more sophisticated numerical model must be utilized.

This investigation involves the analysis and prediction of the nonsteady internal ballistics of a star-grain SRM. The need to include structural vibration within the framework of an internal ballistic simulation model is made evident through observations from previous cylindrical- and star-grain rocket motor research [11,12]. Changes in motor structure (e.g., propellant grain configuration, surrounding wall thickness and material properties) are observed to result in changes in combustion instability symptom profile characteristics (e.g., dual-axial-wave systems vs. single-wave) and magnitude (e.g., dc rise).

2. Numerical model

The numerical model is comprised of two parts or modules – the internal ballistic flow (IBF) and the structural finite element (SFE) module. The IBF model is quasi-one-dimensional in nature, while the SFE module uses a series of two-dimensional finite element (FE) sections placed on the nodes of the IBF grid along the long axis of the motor (refer to Fig. 1). Although the sections are independent of

* Corresponding author.

E-mail address: greatrix@acs.ryerson.ca (D.R. Greatrix).

Nomenclature

A	local core area m^2	r_p	pressure-based burning rate m s^{-1}
a_l	longitudinal acceleration m s^{-2} or g	R	specific gas constant $\text{J kg}^{-1} \text{K}^{-1}$
a_n	normal acceleration m s^{-2} or g	Re_d	local flow Reynolds number
C	pressure-based burning rate coefficient $\text{m s}^{-1} \text{kPa}^{-n}$	t	time s
C_p	gas constant-pressure specific heat capacity $\text{J kg}^{-1} \text{K}^{-1}$	T_f	flame temperature K
C_s	specific heat of propellant (solid phase) $\text{J kg}^{-1} \text{K}^{-1}$	T_s	surface temperature K
[C]	damping matrix	T_i	initial bulk temperature K
d	local core hydraulic diameter m	u	local gas velocity m s^{-1}
E	local total specific energy J kg^{-1}	v_w	flame-front velocity m s^{-1}
f	friction factor	x	axial distance from head-end m
f_i	frequency kHz	{X}	displacement vector
G_a	accelerative mass flux $\text{kg s}^{-1} \text{m}^{-2}$	ΔH_s	net surface heat of reaction J kg^{-1}
G_{a0}	peak accelerative mass flux $\text{kg s}^{-1} \text{m}^{-2}$	Δs	distance between nodes m
k	thermal conductivity $\text{W m}^{-1} \text{K}^{-1}$	β	heat flux coefficient
[K]	stiffness matrix	γ	gas specific heat ratio
[M]	mass matrix	δ_o	reference energy film thickness m
n	pressure-based burning rate exponent	ε	roughness height m
p	local static pressure Pa	ζ	sectional structural damping ratio
P	perimeter length m	κ	local wall dilatation term s^{-1}
Pr	Prandtl number	ξ_L	axial damping ratio of case/propellant
r_b	overall burning rate m s^{-1}	ρ	local gas density kg m^{-3}
r_{b_i}	nodal burning rate m s^{-1}	ρ_s	propellant density kg m^{-3}
r_o	base burning rate m s^{-1}	ϕ_i	power spectral density $\text{MPa}^2 \text{Hz}^{-1}$
		ϕ_d	displacement angle rad
		ω_{nL}	case/prop. natural axial frequency rad s^{-1}
		ω_n	sectional structural resonant frequency rad s^{-1}

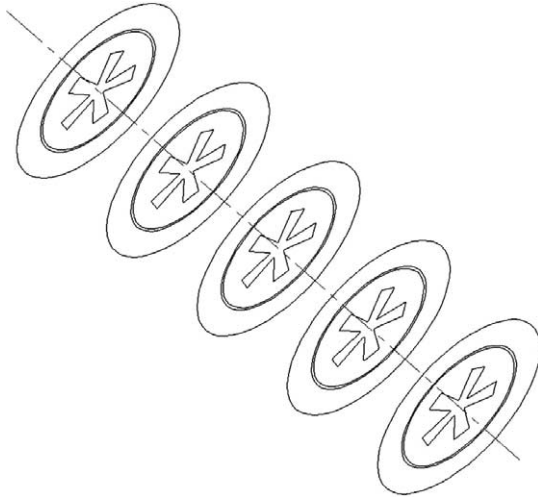


Fig. 1. Simulation model schematic.

each other, they will provide a structural response at every node. Thus an acceleration field will be present to influence the burning rate along the inside boundary of each section.

The quasi-one-dimensional hydrodynamic conservation equations governing the axial gas flow are given below:

$$\frac{\partial \rho}{\partial t} + \frac{\partial(\rho u)}{\partial x} = -\frac{1}{A} \frac{\partial A}{\partial x} \rho u + \rho_s \frac{4r_b}{d} - \left(\frac{4r_b}{d} + \kappa \right) \rho, \quad (1)$$

$$\begin{aligned} \frac{\partial(\rho u)}{\partial t} + \frac{\partial}{\partial x} (\rho u^2 + p) \\ = -\frac{1}{A} \frac{\partial A}{\partial x} \rho u^2 - \left(\frac{4r_b}{d} + \kappa \right) \rho u - \rho a_l, \end{aligned} \quad (2)$$

$$\begin{aligned} \frac{\partial(\rho E)}{\partial t} + \frac{\partial}{\partial x} (\rho u E + up) \\ = -\frac{1}{A} \frac{\partial A}{\partial x} (\rho u E + up) - \left(\frac{4r_b}{d} + \kappa \right) \rho E \\ + \rho_s \frac{4r_b}{d} \left(C_p T_f + \frac{v_w^2}{2} \right) - \rho u a_l. \end{aligned} \quad (3)$$

Note that there are no particulate phase parameters in the above equations, due to the low percentage in the current study; where the solid or liquid phase is substantial, the associated terms can be readily included [7]. In Eqs. (1)–(3), the principal gas flow variables are ρ , p , u , and E , where ρ is the density, p is the pressure, u is the velocity and E is the total specific energy where $E = \frac{p}{(\gamma-1)\rho} + \frac{u^2}{2}$. The additional variables in Eqs. (1)–(3) are the port area (A), hydraulic diameter (d), longitudinal acceleration of the gas (a_l), axial distance from the head end of the motor (x), port dilatation

above that due to propellant regression (κ) where $\kappa = \frac{1}{A} \frac{\partial A}{\partial t}$, flame front velocity (v_w), and propellant burning rate (r_b). C_p , T_f , and ρ_s are constants and refer to the specific heat of the gas, flame temperature and propellant density respectively. These conservation equations are solved using the random-choice method (RCM), which is an explicit, finite-volume integration algorithm for solving systems of hyperbolic equations [4]. The inhomogeneous conservation equations are solved using a generalized higher-order Riemann approach [1,10]. This higher-order method reduces some of the lower-level noise present in the first-order scheme from the source terms.

A quasi-steady (rapid-kinetic-rate) burning rate model is employed for the calculation of the burning rate for any point on the propellant surface. As such, no appreciable lags or overshoots in burning response due to the local flow and vibration conditions occur in the present simulations (there was insufficient experimental information to establish the transient response behaviour that would be applicable; future analyses could include the use of a transient model, e.g., the Zeldovich–Novozhilov [ZN] solid-phase-based burning model [3,15]). The propellant regression rate as described by the phenomenological model is a function of pressure, core flow velocity and acceleration fields present at the burning surface. Erosive burning effects are calculated using [5,9]:

$$r_b = r_0 + \frac{h(T_f - T_s)}{\rho_s [C_s(T_s - T_i) - \Delta H_s]}, \quad (4)$$

where r_0 is the base burning rate component which includes pressure and acceleration effects, C_s is the specific heat of the propellant, T_s is the surface temperature, T_i is the initial propellant temperature, and ΔH_s is the surface heat of reaction of the propellant. The convective heat transfer coefficient (h) is a function of the core flow, and is defined as

$$h = \frac{\rho_s r_b C_p}{\exp\left(\frac{\rho_s r_b C_p}{h^*}\right) - 1}, \quad (5)$$

where

$$h^* = \frac{k}{d} \text{Re}_d \text{Pr}^{1/3} \frac{f}{8}, \quad (6)$$

and

$$f^{-1/2} = -2 \log_{10} \left(\frac{2.51}{\sqrt{f} \text{Re}_d} - \frac{\varepsilon/d}{3.7} \right), \quad (7)$$

where k is the thermal conductivity of the gas, f is the friction factor inside the port, Re_d is the local Reynolds number based on the hydraulic diameter d and the core flow velocity, Pr is the Prandtl number and ε is the surface roughness of the propellant.

Augmentation of the burning rate due to an acceleration field must combine normal, lateral and longitudinal acceleration effects. The combined acceleration augmented burning rate is defined as [6,8]:

$$r_b = \frac{\beta(r_b + G_a/\rho_s)}{\exp[C_p \delta_0 (\rho_s r_b + G_a)/k] - 1}, \quad (8)$$

where β is the heat flux coefficient, δ_0 is the reference energy film thickness and G_a is the accelerative mass flux which are all defined by Eqs. (9), (10) and (11) respectively:

$$\beta = \frac{C_p(T_f - T_s)}{C_s(T_s - T_i) - \Delta H_s}, \quad (9)$$

$$\delta_0 = \frac{k}{\rho_s r_0 C_p} \ln(1 + \beta), \quad (10)$$

$$G_a = \frac{a_n P}{r_b} \frac{\delta_0}{RT_f} \frac{r_0}{r_b}, \quad (11)$$

where a_n is the acceleration normal to the surface and r_0 is the base burning rate which in this instance is due to pressure and core flow effects. The accelerative mass flux defined in Eq. (11) accounts only for accelerations normal to the burning surface. To account for lateral and longitudinal accelerations, a term that considers the orientation of the acceleration vector is required, and is defined by [6]

$$G_a = G_{a0} \cos^2 \phi_d, \quad (12)$$

where G_{a0} is the peak accelerative mass flux defined by Eq. (11), and ϕ_d is the displacement angle and is defined as

$$\phi_d = \tan^{-1} \left[K \left(\frac{r_0}{r_b} \right)^3 \frac{a_l}{a_n} \right], \quad (13)$$

where K is an overall orientation correction factor (experimentally derived) and a_l is the vector sum of the lateral and longitudinal accelerations. K for this study is set at 8 [6]. There is only acceleration-based augmentation when the normal acceleration is negative (into the propellant), such that the combustion layer is being compressed [6]. If the normal acceleration is positive, acceleration effects are assumed to be negligible, conforming to experimental observation [14]. Lateral and longitudinal accelerations are sign-independent and tend to reduce the amount of augmentation produced by the normal acceleration.

Eqs. (4)–(13) are solved iteratively, along with the pressure-dependent burning rate (quasi-steady response via de St. Robert's law, $r_p = Cp^n$; note that in general, the base burning rate r_o for interim burning calculations will incorporate pressure effects and one of either acceleration or core flow effects), to converge to the overall burning rate for any one point on the burning propellant surface. In this type of model, there are many nodes along the interior boundary of the FE grid section. Therefore, the velocity and acceleration-dependent burning rates must converge for each node along the interior boundary of the FE grid. The burning rates for each FE node are used in the burnback routines that regress the propellant grid. For the overall burning rate used in Eqs. (1)–(3), the burning rates are averaged for each section along the IBF grid. The direction of propellant regression for any point along the interior boundary of a section is normal to the local surface [8].

The SFE module uses a nonlinear, large-deformation, plain-strain analysis. All materials are modelled as linearly

elastic, with viscous damping applied to the local structural motion. The Galerkin method is used to discretize the governing differential equations for structural dynamics, over a 3-node constant-strain triangle, resulting in the discrete system [2]:

$$[\mathbf{M}]\{\ddot{X}\} + [\mathbf{C}]\{\dot{X}\} + [\mathbf{K}]\{X\} = [\mathbf{F}], \quad (14)$$

where $[\mathbf{M}]$ is the mass matrix, $[\mathbf{C}]$ is the damping matrix, $[\mathbf{K}]$ is the stiffness matrix, $\{X\}$ is the displacement vector (dotted vectors denote various time derivatives such as velocity and acceleration), and $[\mathbf{F}]$ is the applied external force vector where,

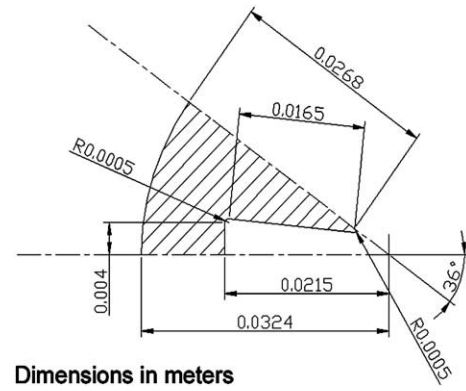
$$[\mathbf{F}] = \sum_{\text{elements}} \left[\iiint_V \rho r \omega^2 dV \right] + \sum_{\text{boundaries}} \left[\iint_S p dS \right]. \quad (15)$$

The force terms in this simulation are the pressure forces along the burning surface and the exterior of the casing (p), and may include centripetal body forces ($\rho r \omega^2$) if considering any spinning of the SRM. There are no point loads or supports, other than those used to prevent lateral rigid-body motion when symmetry is utilized in the FE grid. The mass matrix is lumped and the damping model uses the simple relationship [13]:

$$[\mathbf{C}] = 2\zeta \omega_n [\mathbf{M}], \quad (16)$$

where ζ is the structural damping ratio and ω_n is the fundamental resonant frequency of the 2-D section. This allows an explicit central difference method to be used to solve Eq. (14). An explicit method is desirable for this simulation as the IBF module is also explicit; an implicit FE method would be computationally wasteful in this application, as the time step would be limited by the explicit IBF solver.

The boundary conditions for both the IBF calculations and the SFE calculations are what couple the two solutions. Output from the IBF solver in terms of local chamber pressure and burning rate provide boundary conditions (along with those to prevent lateral rigid body motion) for the SFE and propellant regression calculations. The chamber pressure, having only one value at any one section, is constant around the internal boundary of a given section, while the burning rate has a unique value for every node around the internal boundary. This is true for every section along the axis of the grain. In turn, output from the SFE solver in the form of port geometry, and lateral and normal accelerations, provide boundary conditions (along with a zero-velocity boundary condition at the head-end of the motor) for the IBF and burning rate calculations. While the IBF solver calculates the burning rate for every node of the section to return to the propellant regression algorithm, the value of r_b used in the IBF calculations uses an value averaged over the perimeter of the section (i.e., $r_b = \sum r_{b_i} \Delta s / P$, where r_{b_i} is the burning rate at a node in the section, Δs is the distance between nodes in the section and P is the perimeter of the internal boundary of the section). The initial conditions of the unsteady calculations consist



Dimensions in meters

Fig. 2. Star-grain geometry details.

of pressurizing the motor to the design chamber pressure value, then running quasi-steady IBF calculations along with the propellant regression algorithm to simulate the steady operation of the motor prior to introducing the non-steady calculations at a predetermined time.

An unstructured triangular grid is used which contains the propellant in an aluminium casing surrounded by a thick steel sleeve (refer to Fig. 3). A typical flight-ready SRM does not include this sleeve, but a steel sleeve may be fitted to motors mounted on a test stand, for safety. The grid for the propellant is generally created finer than that of the casing for two reasons. First, the acceleration field must be accurately calculated along the burning surface to be able to sufficiently model the coupling of structural vibrations with the burning rate. Second, the grid should be fine enough such that as the burning surface regresses, the accuracy of the port geometry (port area, perimeter length, etc.) is maintained.

The star-grain propellant geometry is based on SRMs similar to those motors used in [12]. This geometry is dimensioned in a pie section as illustrated in Fig. 2. The star-grain geometry exhibits symmetry, so to save on computer time a motor section is broken up into pie slices. Fig. 3 displays a 1/10th pie section of the FE grid including a 1.27 mm aluminum casing (darkest shade of colour) and a 14.1 mm steel sleeve (medium shade, to the right of casing); the propellant being the lightest shade, to the left of casing). The arrows along the propellant burning surface denote the direction of propellant regression.

As a final note, in order to initiate instability in the motor, a traveling wave pulse is introduced into the core flow at a predetermined time. This disturbance consists of a compression wave front and an expanding tail. In order to be consistent with previous experimental tests [12], the motor will be pulsed when 28% of the total propellant by mass has burnt away. Therefore, the FE grid will look comparable to the grid shown in Fig. 4. Since the propellant will regress at various rates along the motor length, the actual grid may vary somewhat from the one displayed in Fig. 4, depending on the section location. Note that the actual grid used for the results displayed later in this paper had a much higher element density; it is too dense to be printed here.

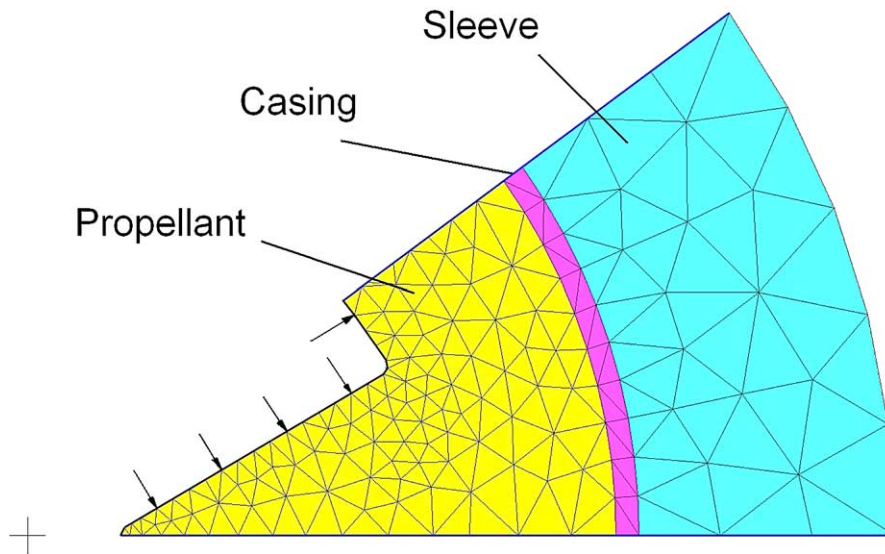


Fig. 3. 1/10th pie section of FE grid.

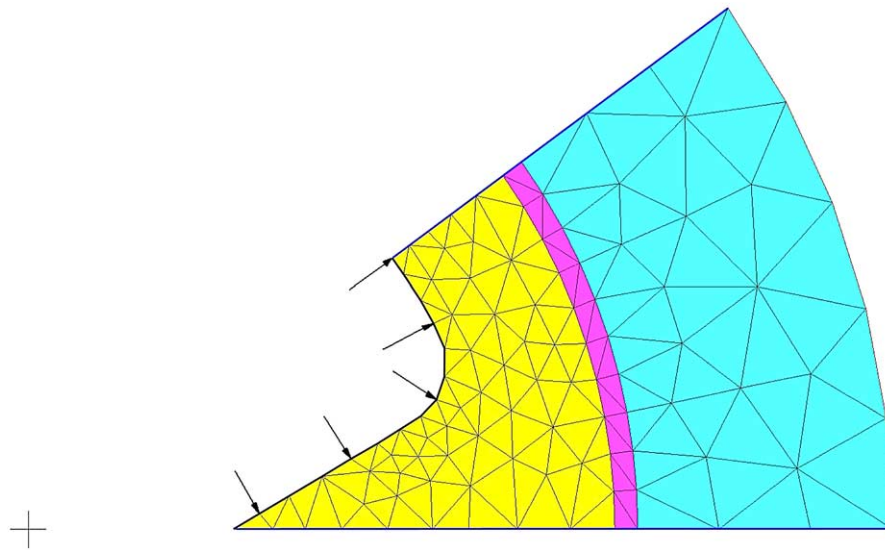


Fig. 4. FE grid at 28% burnback.

3. Simulation predictions

The propellant characteristics used in these simulations are typical for a nonaluminized ammonium perchlorate/hydroxyl-terminated-polybutadiene propellant. These characteristics are listed in Table 1. Net surface heat release ΔH_s is set to zero to produce steady-state erosive and acceleration-based burning model results consistent with experimental observation for a wide range of solid propellants [5,6,8,9]. Note that the FE fundamental resonant frequency in Table 1 is a value found from an eigenvalue analysis of the 2D SRM section at the mid-point of the motor at 28% total propellant mass fraction. The star-grain geometry has two principal resonant frequencies, one for the peak of the star (thickest web) at about 4200 Hz, and one at the trough (thinnest web) at about 14000 Hz. Using the lower

natural frequency as the fundamental resonant frequency in the damping model will result in the peak of the star grain being properly damped (as expected from the employed damping ratio) and the trough of the star-grain being under-damped. In order to maintain a consistent amount of damping throughout the section such that the system responds as expected for a given damping ratio, the algorithmic damping constant, which filters higher frequency oscillations, is increased somewhat to help damp the higher frequency vibrations in the trough of the star grain (refer to Fig. 5). Doing so will make the damping consistent throughout the system using the lower principal frequency. The fundamental resonant frequency in Table 1 is applied to every section for the damping model. This is reasonable since the fundamental resonant frequency will not vary too much from section to section.

Table 1

Reference SRM characteristics

FE fund. resonant frequency (ω_n)	4199 Hz
FE damping ratio (ζ)	0.25
Prop. elastic modulus (E_{Prop})	45 MPa
Prop. Poisson's ratio (ν_{Prop})	0.497
Propellant density (ρ_{Prop})	1730 kg m ⁻³
Casing elastic modulus (E_{AI})	80 GPa
Casing Poisson's ratio (ν_{AI})	0.33
Casing density (ρ_{AI})	2700 kg m ⁻³
Casing thickness (t_{AI})	1.27 mm
Casing inner wall radius (r_{AI})	32.4 mm
Sleeve elastic modulus (E_{SI})	200 GPa
Sleeve Poisson's ratio (ν_{SI})	0.3
Sleeve density (ρ_{SI})	7850 kg m ⁻³
Sleeve thickness (t_{SI})	14.1 mm
Sleeve inner wall radius (r_{SI})	33.67 mm
Propellant grain length (L_p)	518 mm
Nozzle throat diameter (d_t)	23 mm
Grain/nozzle conv. length ratio (L_p/L_c)	16
Press.-dep. burn rate (r_p)	0.0007[p(kPa)] ^{0.35} m s ⁻¹
Propellant specific heat (C_s)	1500 J kg ⁻¹ K ⁻¹
Propellant flame temp. (T_f)	3000 K
Propellant surface temp. (T_s)	1000 K
Initial propellant temp. (T_i)	294 K
Propellant surf. roughness (ϵ)	10 μ m
Gas specific heat (C_p)	1920 J kg ⁻¹ K ⁻¹
Gas Prandtl number (Pr)	0.72
Specific gas constant (R)	320 J kg ⁻¹ K ⁻¹
Gas thermal conductivity (k)	0.2 W m ⁻¹ K ⁻¹
Gas absolute viscosity (μ)	8.075 $\times 10^{-5}$ Pa s
Gas specific heat ratio (γ)	1.2
Casing/prop. long. damping ratio (ξ_L)	0.1

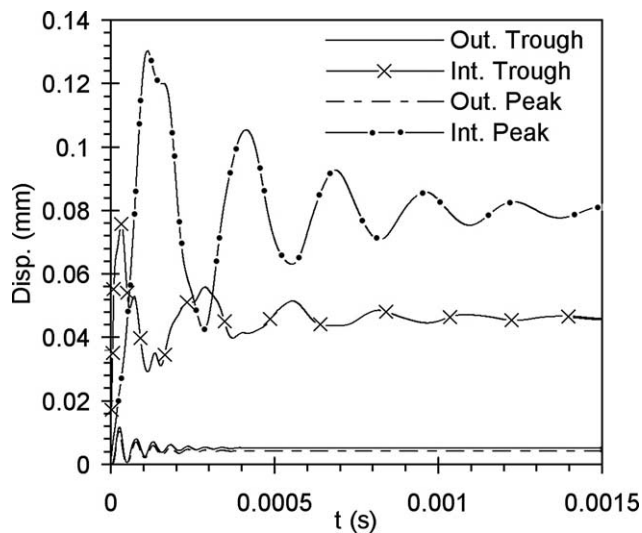


Fig. 5. Displacement-time plot for 10.5-MPa step impulse.

For the case studied, the SRM is pulse-triggered into instability using a 0.71 MPa overpressure pulse ($\sim 5\%$ of the base chamber pressure), introduced at 158 ms into the simulated firing. Fig. 6 displays the head-end pressure-time profile for this simulation run. The limiting wave amplitude reaches a value of approximately 4 MPa soon after the pulse is triggered (cycling at a frequency of about 1 kHz, which

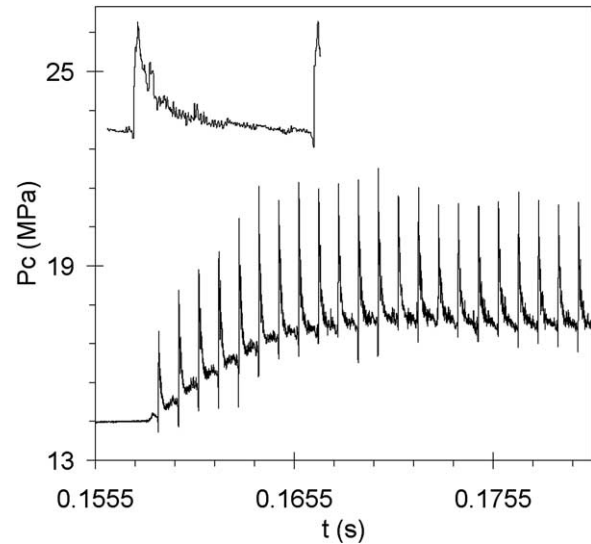


Fig. 6. Head-end pressure-time profile.

corresponds to the axial acoustic frequency of the motor chamber), and the base pressure increases to a value of ~ 17.5 MPa, a dc rise of ~ 3.5 MPa. The pulsing time and resulting dc shift are comparable to the time-averaged star-grain SRM data presented in [12].

The star-grain propellant structure will generally have a greater number of significant vibration modes than cylindrical-grain motors. Of particular interest are the regions of the trough and the peak of the propellant inner surface (refer to Fig. 3 or Fig. 4). These two regions have differing natural frequencies as Harris, Wong and de Champlain also noted in their FE structural analysis [12], and so will affect the coupling of the structural vibrations to the burning rate. Looking at the inset of Fig. 6, one cycle of a wave at a later time (approaching limit amplitude) is displayed. In comparison to the numerical cylindrical-grain SRM results seen in [11], there is more post-shock activity present in Fig. 6. The higher frequency oscillations in the trough of the grain section would appear, through the acceleration-augmented burning rate mechanism, to especially reinforce the secondary waves after the initial shock front has passed, in addition to burning input from the peak section of the grain. The coupling of local propellant surface vibrations to the burning rate is discussed further in this paper.

Figs. 7 and 8 display the normal acceleration-time graphs for the trough and peak respectively, of the inner propellant surface at the mid-point of the SRM. Here, it is evident that there is more activity in the trough of the section than the peak. The peak acceleration levels approach ± 55000 g in Fig. 7 while they reach ± 45000 g in Fig. 8. Looking at the insets in Figs. 7 and 8 which display one later limit-amplitude cycle of the pressure wave arising from the head-end location, it can be seen that there is more activity in the post-shock oscillations in the trough. This suggests that there is more burning rate augmentation in the troughs than at the peaks as a result.

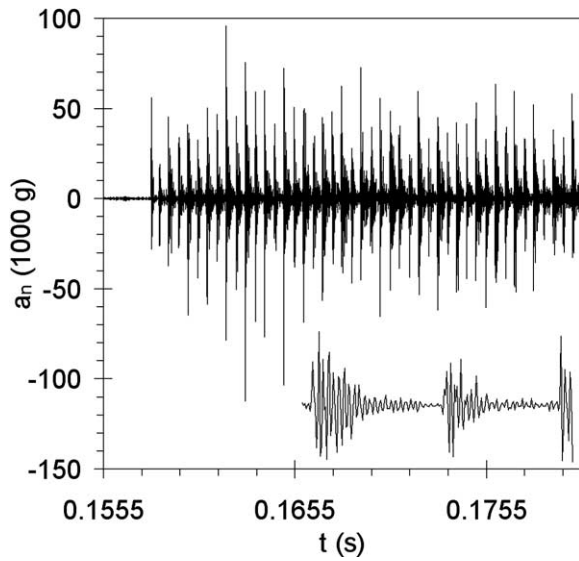


Fig. 7. Mid-point normal acceleration at the trough of the inner propellant surface.

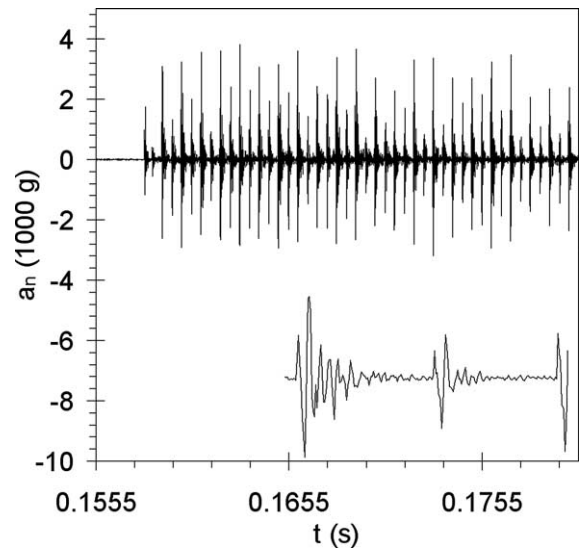


Fig. 9. Mid-point normal acceleration at the sleeve external wall over the trough of the star-grain section.

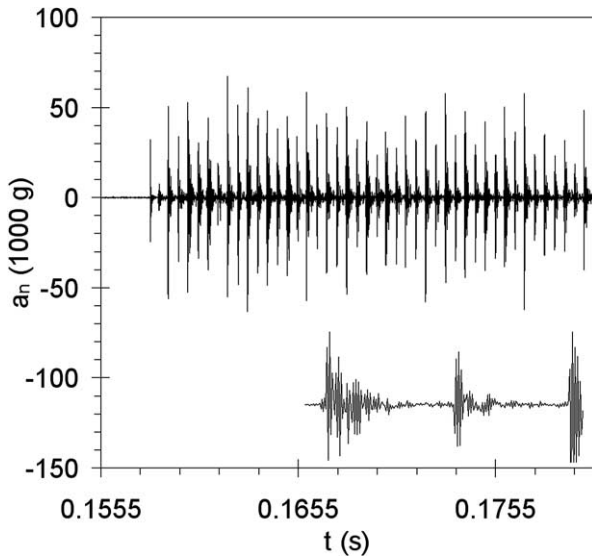


Fig. 8. Mid-point normal acceleration at the peak of the inner propellant surface.

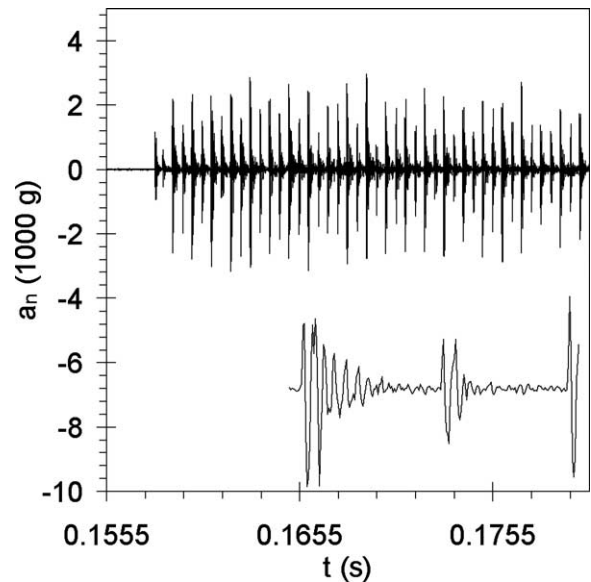


Fig. 10. Mid-point normal acceleration at the sleeve external wall over the peak of the star-grain section.

The mid-length sleeve external wall accelerations for positions directly over the trough and peak are displayed in Fig. 9 and Fig. 10 respectively. The insets correspond to those for Figs. 7 and 8. Again, variations in the peak acceleration levels are evident; Fig. 9 having peak levels of ± 3000 g and Fig. 10 having peak levels of ± 2500 g.

In order to examine the coupling of the structural vibrations with wave development, a displacement-time plot of one cycle at the mid-length is displayed in Fig. 11 along with the mid-length chamber pressure in Fig. 12. The higher frequency oscillations of the trough region are evident in Fig. 11. The principal frequency of the peak region of the resonant frequency of the motor section (~ 4 kHz), while the principal frequency of the trough region of the star grain is higher at ~ 14 kHz; this will correlate to larger local

accelerations in the trough, thus leading to a higher burning rate augmentation via the mechanisms presented through Eqs. (8)–(13).

The grain section peak has a lesser role in the burning rate with a lower vibration frequency and comparable deflection. The lower vibration frequency produces a longer period where the local accelerations augment the burning rate to a lesser degree than the trough, due to the lower mean amplitude. The net effect of the overall burning rate input is evident in the inset of Fig. 6 and in Fig. 12, where the post-shock pressure does not decay immediately to the base pressure level, as observed by Greatrix and Harris for the numerical results for a cylindrical-grain SRM [11].

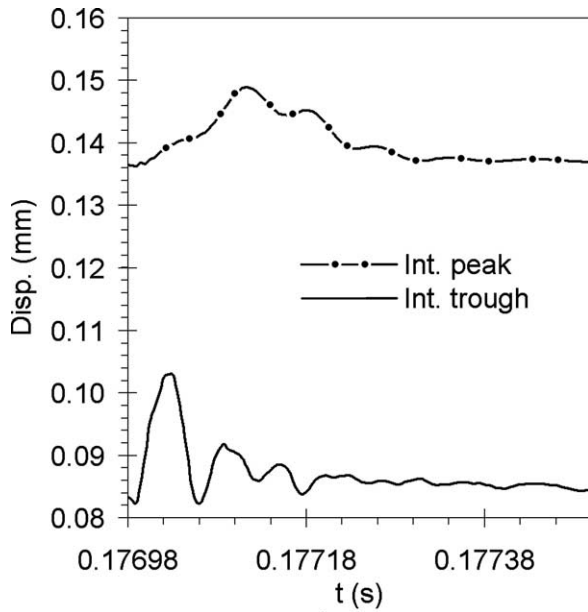


Fig. 11. Mid-point displacement of inner propellant surface.

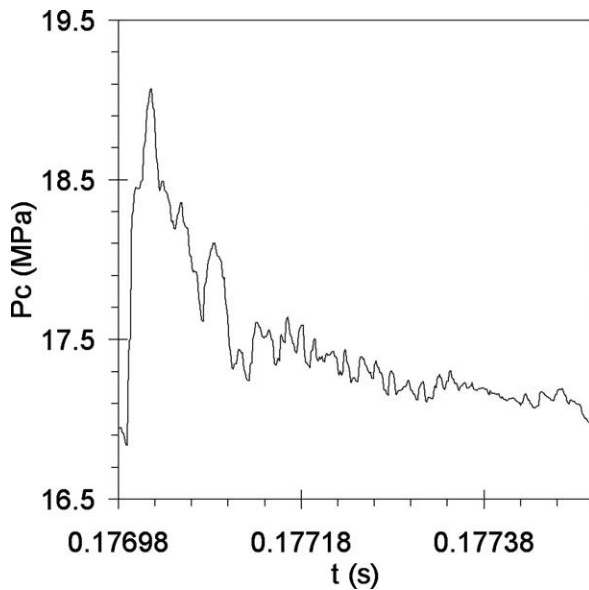


Fig. 12. Mid-point chamber pressure.

The power spectral density (ϕ_i) of the head-end pressure data shown in Fig. 6 is displayed in Fig. 13 (sampled at a later time, when the pressure cycle has reached a quasi-equilibrium limit-amplitude status). Here we see that the first prominent frequency corresponds to the fundamental axial resonant frequency of the motor (~ 1 kHz). The next spike (2 kHz) is a little stronger than the first, possibly because of contributions from the axial vibration of the motor on the load-cell/test stand (this vibration has a frequency of ~ 2 – 4 kHz). It is clear that most of the activity lies in the frequencies below 5 kHz. However, the graph shows that there is an increase of activity in the region of 14 kHz. This could possibly correspond to the burning rate

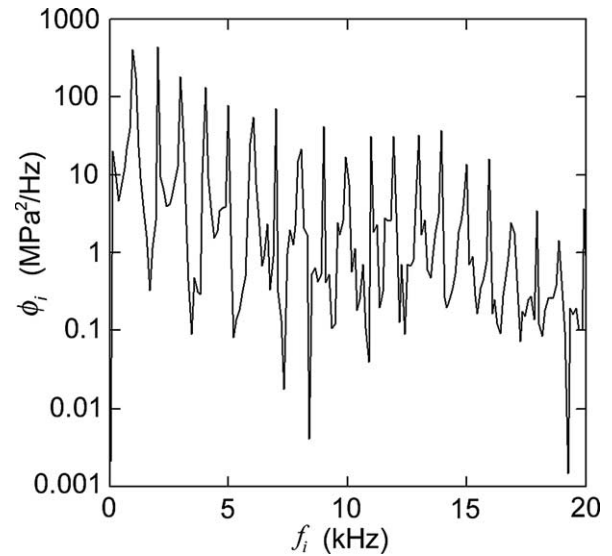


Fig. 13. Power spectral density profile, for limit-amplitude head-end pressure.

augmentation in the trough of the star grain, which oscillates at approximately this frequency.

4. Concluding remarks

The ability of this numerical simulation model to describe star-grain SRM axial instability behaviour has been demonstrated. Although there was no high-resolution experimental data to compare to, the numerical output does correlate to the time-averaged results, indicating a comparable dc shift in chamber pressure [12]; experimental data for high-frequency pressure and motor wall acceleration is required for further validation. One of the key factors affecting wave development in the star-grain motor is the vibration of the peak and trough of the star geometry. Each region oscillates at a different frequency; therefore, each region affects pressure wave development to a level that depends on the dynamic response of that region. Since the trough generally oscillates at a higher frequency at deflection amplitudes comparable to the section peak, the local acceleration field will tend to be stronger, reinforcing the passing shock wave and generating secondary pressure waves behind the shock front. The peak of the star geometry tends to oscillate at a lower frequency, and thus appears to augment the burning rate to a lesser degree over a longer period. This would appear to reduce the post-shock pressure decay in the pressure wave.

This numerical model predicts SRM combustion instability symptoms based on an acceleration-augmented burning rate mechanism, independent of any additional transient pressure- or velocity-coupled augmented combustion driving mechanism. Axial vibration is not a strong factor in this study due to the comparatively small axial acceleration levels, given the heavyweight motor system on the test stand [11]. Other sources of acceleration fields lie in structural vi-

brations affected by transverse waves. Although not modeled in this simulation, transverse waves could play an important role in star-grain internal ballistic behaviour. This may be especially the case early on in the firing where transverse wave vibration frequencies may lie closer to the natural frequency of the trough region; so, even if the trough region has a higher damping coefficient, transverse wave activity may augment existing structural vibrations to negate the effect of greater damping, and further enhance wave development.

Acknowledgement

This work has been supported by funding from the Natural Sciences and Engineering Research Council of Canada.

References

- [1] M. Ben-Artzi, J. Falcovitz, An upwind second order scheme for compressible duct flows, *SIAM J. Scientific Statist. Comp.* 7 (3) (1986) 768–774.
- [2] R.D. Cook, D.S. Malkus, M.E. Plesha, R.J. Witt, *Concepts and Applications of Finite Element Analysis*, 4th Ed., Wiley, New York, 2002.
- [3] L. De Luca, E.W. Price, M. Summerfield (Eds.), *Nonsteady Burning and Combustion Stability of Solid Propellants*, *Progress in Astronautics and Aeronautics*, vol. 143, AIAA, 1992.
- [4] J. Glimm, Solutions in the large for nonlinear hyperbolic systems of equations, in: *Communications in Pure and Applied Mathematics*, Vol. 18, 1965, pp. 697–715.
- [5] D.R. Greatrix, Parametric analysis of solid-propellant erosive burning, *CSME Forum*, June 27–29, 1994.
- [6] D.R. Greatrix, Parametric analysis of combined acceleration effects on solid-propellant combustion, *Canadian Aeronautics Space J.* 40 (2) (1994) 68–73.
- [7] D.R. Greatrix, Structural vibration and solid rocket combustion instability, *Canadian Aeronautics Space J.* 44 (1) (1998) 9–24.
- [8] D.R. Greatrix, Acceleration-based combustion augmentation for non-cylindrical grain solid rocket motors, *AIAA Paper No. 95-2876*, July 10–12, 1995.
- [9] D.R. Greatrix, J.J. Gottlieb, Erosive burning model for composite-propellant rocket motors with large length-to-diameter ratios, *Canadian Aeronautics Space J.* 33 (3) (1987) 133–142.
- [10] D.R. Greatrix, J.J. Gottlieb, Higher-order random-choice method for internal ballistic flows, *CFD99*, May 30–June 1, 1999.
- [11] D.R. Greatrix, P.G. Harris, Structural vibration considerations for solid rocket internal ballistics modeling, *AIAA Paper No. 2000-3804*, July 17–19, 2000.
- [12] P.G. Harris, F.C. Wong, A. de Champlain, The influence of structural vibrations on pulse-triggered nonlinear instability in solid rocket motors: an experimental study, *AIAA Paper No. 96-3250*, July 1–3, 1996.
- [13] L. Meirovitch, *Fundamentals of Vibration*, McGraw-Hill, New York, 2001.
- [14] E.J. Sturm, R.E. Reichenbach, An investigation of the acceleration induced burning rate increase of non-metallized composite propellants, *AIAA J.* 8 (6) (1970) 1062–1067.
- [15] V. Yang, T.B. Brill, W.Z. Ren (Eds.), *Solid Propellant Chemistry, Combustion, and Motor Interior Ballistics*, *Progress in Astronautics and Aeronautics*, vol. 185, AIAA, 2000.